



Design of crack-free laser additive manufactured Inconel 939 alloy driven by computational thermodynamics method

Congyuan Zeng¹, Huan Ding, Uttam Bhandari, S. M. Guo, Department of Mechanical & Industrial Engineering, Louisiana State University, Baton Rouge, LA 70803, USA

Address all correspondence to Congyuan Zeng at czeng8@lsu.edu

(Received 3 April 2022; accepted 25 August 2022; published online: 9 September 2022)

Abstract

This paper examined the effect of Si addition on the cracking resistance of Inconel 939 alloy after laser additive manufacturing (AM) process. With the help of CALculation of PHase Diagrams (CALPHAD) software Thermo-Calc, the amounts of specific elements (C, B, and Zr) in liquid phase during solidification, cracking susceptibility coefficients (CSC) and cracking criterion based on $|dT/df_s^{1/2}|$ values (T : solidification temperature, f_s : mass fraction of solid during solidification) were evaluated as the indicators for composition optimization. It was found that CSC together with $|dT/df_s^{1/2}|$ values provided a better prediction for cracking resistance.

Introduction

Laser powder bed fusion (L-PBF) additive manufacturing (AM) has been applied rapidly to various fields such as aerospace^[1] and automation^[2] for its unique capability to produce components with complex shapes and high dimensional accuracy, which are almost impossible with conventional subtractive fabricating strategies.^[3] Up to now, a few categories of metals and alloys have been widely investigated with L-PBF process, for example Ti-6Al-4V,^[4] Inconel 718,^[5] Inconel 625,^[6] stainless steel 316L^[7] and CuCrZr alloy.^[8] L-PBF process typically requires weldable alloys as the feedstock material. However, due to the poor weldability, many alloys are deemed not suitable for L-PBF process.

Inconel 939 alloy is unfortunately within the category of non-weldable alloys for L-PBF process despite its outstanding properties,^[9] i.e., high creep resistance, excellent corrosion/oxidation resistance, and high-temperature microstructure stability.^[10–12] The primary cracking mechanism for Inconel 939 alloy is believed to be solidification cracking that usually occurs close to the end of solidification stage as the liquid feed in the inter-dendritic region is constrained.^[13,14] It is reported that during welding process of Inconel 939 alloy, the boundary strengthening elements, i.e., C, B and Zr, segregate to inter-dendritic regions and form low-melting-point liquid films, which can be pulled apart by tensile stress generated due to the restriction of substrates during solidification.^[9] Therefore, reducing the amounts of the boundary strengthening elements at the final solidification stage could be a feasible way to improve the cracking resistance of Inconel 939 alloy. This strategy has been applied by other researchers to improve the solidification cracking resistance of 310 stainless steel^[15] and transformation-induced plasticity steels.^[16] The addition of Si has been reported to improve the weldability of Al alloys, making them suitable for L-PBF process, i.e., AlSi7Mg0.6,^[17]

Al-12Si alloy,^[18] Al10SiMg alloy^[19] and 4 wt%Si + Al7075 alloy.^[20] In view of those prior research work, the effect of Si addition on improving the cracking resistance of Inconel 939 alloy processed by laser AM conditions is examined in this paper. The design of Inconel 939 alloy with Si addition in this study was undertaken by Thermo-Calc simulations. The composition of liquid phase during solidification was explored with Scheil Solidification Simulation Model, especially for elements C, B, and Zr. Those elements tend to form low-melting-point liquid phases.^[9,21] The lower contents of C, B, and Zr elements at the final stage of solidification are expected to lead to lower amounts of low-melting-point phases, resulting in higher cracking resistance.^[9,15,16] In addition, experimental work was performed to verify the Thermo-Calc simulation results.

Simulation and experiments

Solidification cracking is closely related to the final stage of solidification.^[22] Due to the fast solidification rate, it is extremely challenging to investigate composition information during laser based additive manufacturing experimentally. Therefore, Thermo-Calc software was applied to predict concentrations of C, B, and Zr elements in liquid phase during solidification, cracking susceptibility coefficients (CSC) and $|dT/df_s^{1/2}|$ values (T : solidification temperature, f_s : mass fraction of solid during solidification) for Inconel 939 alloys with different Si additions using the TCNI8:Ni Alloys v8.2 database. Scheil Solidification Simulation model was applied to simulate the fast solidification process in this study, and B, C elements were considered as fast diffusers.^[23] For not changing the composition of Inconel 939 alloy significantly, Si addition during Thermo-Calc calculation was limited to be below 10 wt%.

Commercial spherical shaped Inconel 939 powders and pure Si powders (99.5% purity) were used as raw materials. Composition of the Inconel 939 alloy is Ni-23.23Cr-19.31Co-3.83Ti-1.85Al-1.83W-1.37Ta-1.04Nb-0.20Fe-0.16Mo-0.14C-0.10Zn-0.01B (wt%). In this study, five compositions were selected for experimental verification, namely pure Inconel 939 alloy and Inconel 939 alloy with Si additions of 0.5, 1, 3, and 8 wt%. Hereafter, the samples were denoted as Ni939, Ni939+0.5Si, Ni939+1Si, Ni939+3Si, and Ni939+8Si, respectively. MAM-1 Arc melter was utilized to synthesize Inconel 939 alloy samples with and without Si addition under pure argon. The samples were subsequently cut by a BUEHLER low speed saw to expose the cross sections, which then were mechanically ground with SiC papers up to 600 mesh. A custom laser processing system was utilized to mimic the L-PBF process over the cross sections. The applied parameters include laser power (95 W), scanning speed (100 mm/s), hatch space (50 μm), spot size (46 μm) and a pure argon environment. Detailed description of the laser system setup can be found elsewhere.^[24] A field emission scanning electron microscope (SEM) equipped with energy dispersive spectroscopy (EDS) detector was used to observe the laser irradiated surfaces and their compositions. A software named ImageJ was applied to quantitatively measure the crack densities on the laser processed surfaces.

Results and discussion

Figure 1 shows the variation behaviors of the contents of C, B, and Zr in liquid phase during solidification process obtained with Thermo-Calc prediction. Generally, the three elements show different variation behaviors.

When the addition of Si is below 1 wt%, the amount of C increases first and then monotonically decreases as f_s rises. However, when the addition of Si is over 3 wt%, C content first quickly declines, and then decreases with a much slower rate. This phenomenon is ascribed to the generation of FCC_L12#3 phase (containing ~ 14.5 wt% C) [Fig. 1(a)]. When Si addition is below 1 wt%, an earlier formation of FCC_L12#3 phase effectively reduces C contents in the liquid phase. With an addition of Si over 3 wt%, FCC_L12#3 phase forms at the beginning of solidification process, and a higher Si addition helps to generate more FCC_L12#3 phase and brings C content to a significantly lower level compared with other counterparts over the entire solidification process.

Similar with the C element case, the Ni939+8Si sample contains clearly the lowest B element content in liquid phase over the entire solidification stage. For the rest samples, when f_s is below 0.851, the variation curves perfectly overlap with one another. With the increase of Si addition, the point that B concentration starts to decline appears at earlier stage of solidification [Fig. 1(b)]. This observation is ascribed to the generation of MB2_C32 phase, which is a Ti-B phase containing 31 wt% of B. Therefore, an increased addition of Si can

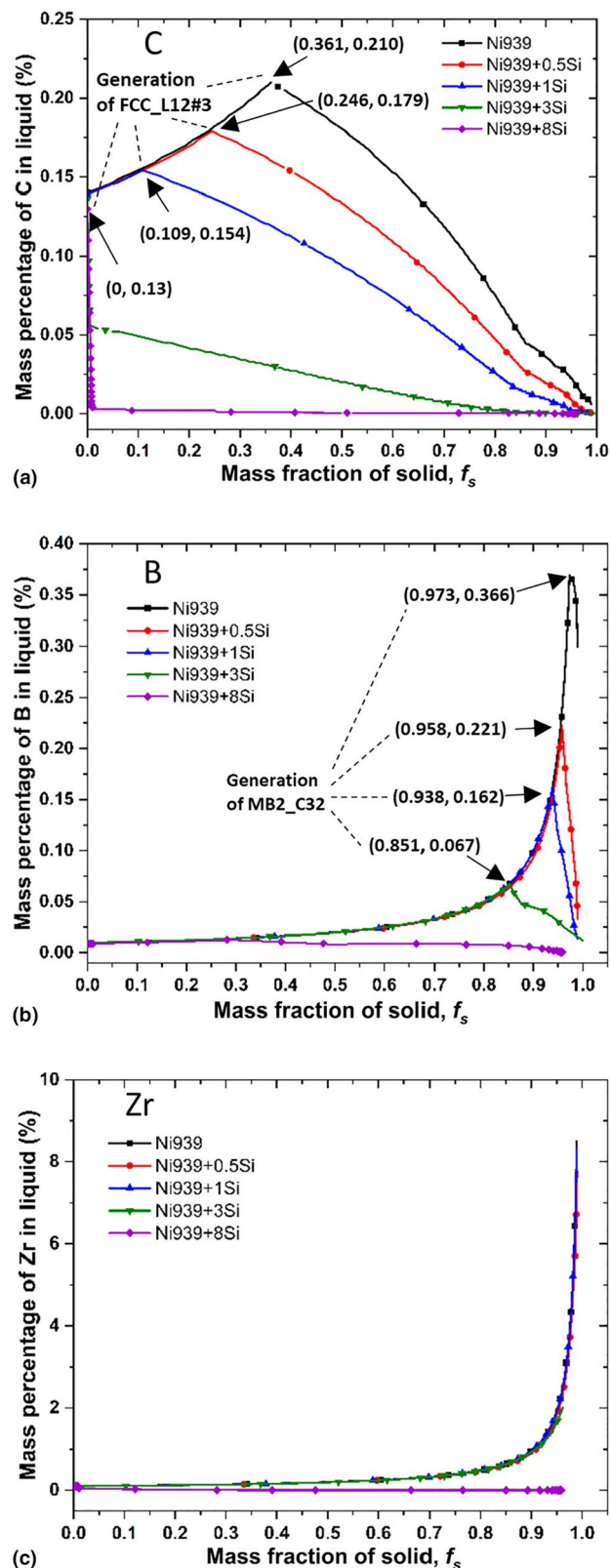


Figure 1. Contents of C, B and Zr elements in liquid phase during solidification process predicted by Thermo-Calc.

effectively reduce B concentration in liquid phase close to the end of solidification stage for the Inconel 939 alloy. Again, Zr amount in liquid phase for Ni939+8Si sample shows the lowest value over the whole solidification process, while Zr amounts for the rest samples in liquid phase increases exponentially. With a careful observation, the variation curves of Ni939, Ni939+0.5Si, and Ni939+1Si nearly overlap each other, with the final concentration around 8 wt%, while the sample Ni939+3Si shows a lower value of 2 wt%.

Apparently, C, B, and Zr contents in liquid phase during solidification are Si addition dependent. With the increase of Si addition, significant lower amounts of C, B, and Zr are observed at the final stage of solidification. If the cracking susceptibility was solely determined by the levels of C, B, and Zr in the liquid near the completion of the solidification process, one would conclude that Ni939+8Si alloy would show the lowest crack density compared with other samples. To verify this hypothesis, experimental study was performed on four selected samples, namely Ni939, Ni939+1Si, Ni939+3Si, and Ni939+8Si.

Figure 2(a) shows the representative surface morphology of Ni939 sample both before and after laser irradiation. Based on this image, no visible cracks can be seen in arc-melted region, while large amounts of cracks are observed in laser irradiated region [representatively indicated by the white arrows in Fig. 2(a)]. During arc melting process, the feedstock is melted and forms a button-shaped melt due to surface tension. Considering that solidification cracking is caused by the combination of low-melting-point liquid films

in the inter-dendritic regions and tensile stress, it is deduced that the thermal stress inside the arc-melted sample is not large enough to generate cracks. However, under laser AM process on substrates, due to the restriction of the substrate during solidification of the narrow molten tracks, the laser scanned top surface layer usually experiences large tensile stress, leading to cracking if the material shows poor weldability.^[25,26]

EDS characterization was performed to determine the real surface compositions of laser irradiated parts, and Si contents for the four samples are 0 , 1.5 ± 0.05 wt%, 2.8 ± 0.1 wt%, and 7.4 ± 0.21 wt%, respectively. For better distinguishing, the four samples are denoted as Ni939, Ni939+1.5Si, Ni939+2.8Si, and Ni939+7.4Si, respectively.

Surface morphologies of the selected four samples after laser irradiation are shown in Fig. 2(b)–(e). Clearly, when the Si addition increases to 2.8 wt%, crack density decreases, and no visible cracks are observed in the Ni939+2.8Si sample, which indicates a significant improvement of cracking resistance. With a careful observation, cracks in the Ni939+1.5Si sample are shorter than those in the Ni939 sample. The Ni939+7.4Si sample contains clearly higher amounts of cracks than any other samples. This indicates that when the Si addition reaches 7.4%, weldability of the material sharply declines. ImageJ software was used to quantify the crack density on the four sample surfaces, and the average crack densities of Ni939, Ni939+1.5Si, Ni939+2.8Si, and Ni939+7.4Si are approximately 2.46, 1.75, 0, and 9.07 mm/mm², respectively. The results observed in Fig. 2(b)–(e) shows that

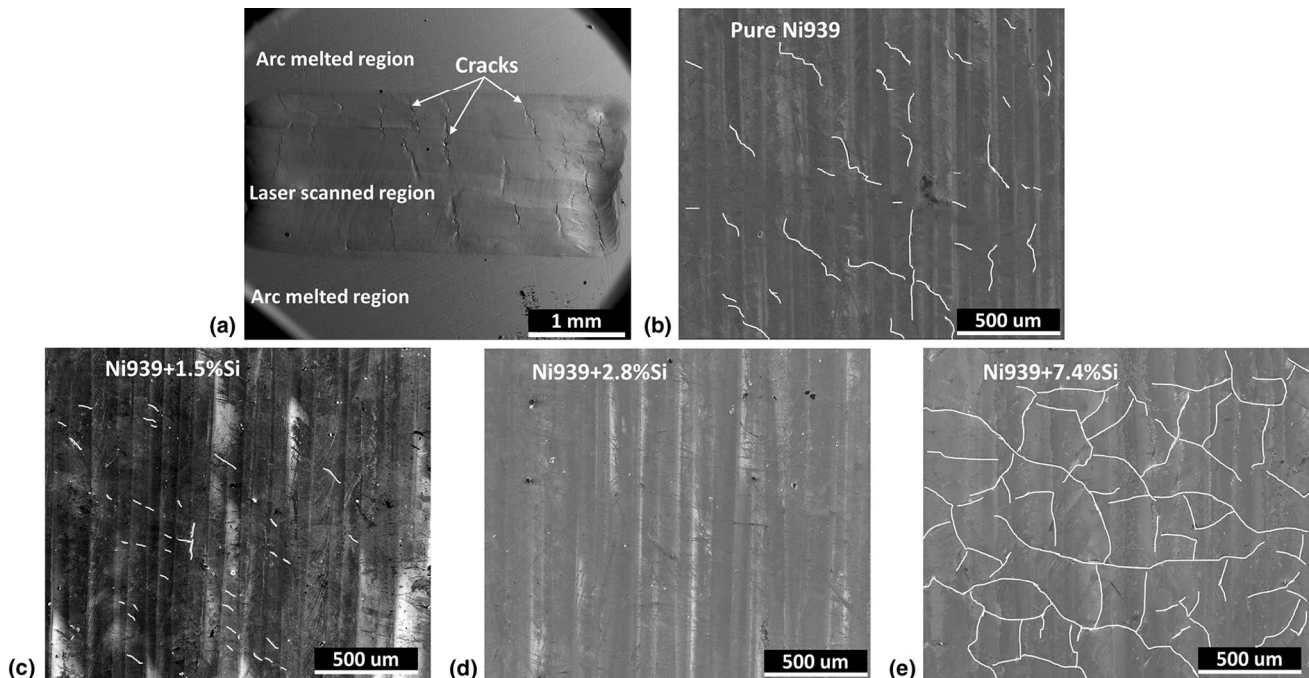


Figure 2. (a) SEM image showing the surface morphologies of arc-melted region and laser scanned region of Ni939 sample. (b)–(e) SEM images indicating the surface morphology of the samples after laser irradiation. The cracks were highlighted with white curves for easier observation.

cracking susceptibility cannot be determined solely by the levels of C, B, and Zr in the liquid near the completion of the solidification process.

The primary cracking mechanism of Inconel 939 alloy was reported solidification cracking.^[9] Quantitative prediction of solidification cracking tendency named CSC was recently offered by Thermo-Calc software based on the research by Clyne and Davies.^[27] CSC depends on critical times during solidification. A smaller CSC value indicates the material less prone to cracking, and vice versa. The calculation of CSC uses Scheil Solidification Simulation Model combined with a heat flow model proportional to $1/t^{1/2}$ (t represents time).^[28] Scheil Model predicts solidification temperature ranges without considering time, while the heat flow model introduces time to the calculation. Solidification cracking happens in the later stage of solidification. With a liquid phase amount in the range from 60 to 10%, adequate liquid feeding to the grain gaps caused by thermal contraction makes the material less prone to cracking, and the duration of this period is named the relaxed period, t_R . With a liquid amount in between 10 and 1%, the material is vulnerable to cracking due to limited liquid feeding,^[29] and the duration over this stage is t_V . With combined solidification and heat flow models, CSC is defined in Formula (1). Detailed description on the calculation of t_V and t_R can be found elsewhere.^[29]

$$\text{CSC} = t_V/t_R \quad (1)$$

CSC values of Inconel 939 alloy with up to 10 wt% Si additions are shown in Fig. 3(a). Clearly, CSC goes up quickly as Si addition increases to 0.5 wt%, then decreases rapidly when Si addition further rises to 2.5 wt%. When Si addition is within the range of 2.5–5 wt%, CSC value remains at a low level. CSC increases to 0.8 as Si addition rises to 6–7 wt%, then quickly increases to 4.4 when Si addition reaches 8 wt%. After that, CSC values gradually decreases. The CSC values for points a, b, c and d in Fig. 3(a) are listed in Table I, which is generally

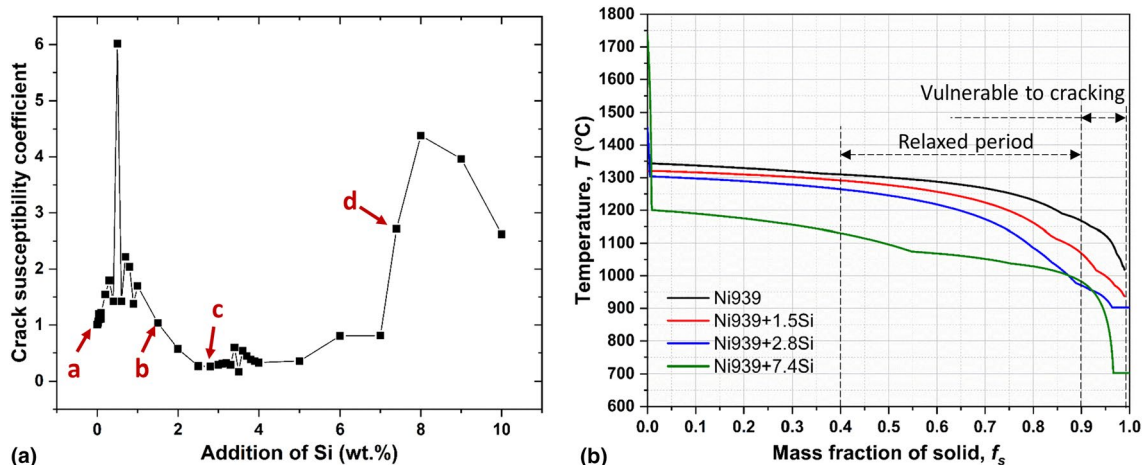


Figure 3. (a) Image showing the cracking susceptibility coefficient (CSC) as a function of Si element addition, a, b, c, d indicate the CSC corresponding to the four samples experimentally tested. (b) Solidification ranges of the four samples, T vs. f_s .

Table I. Calculated cracking tendencies based on CSC and strain rates for the samples

Sample name	Composition point	CSC	$ dT/df_s^{1/2} $ (°C)	Critical f_s
Ni939	a	1.006	9950	0.989
Ni939+1.5Si	b	1.038	7956	0.989
Ni939+2.8Si	c	0.263	5323	0.964
Ni939+7.4Si	d	2.717	57,341	0.966

in good accordance with the crack densities observed in Fig. 2. According to Fig. 3(a), CSC is Si addition dependent and the Si addition range of 2.5–5.0 wt% leads to low CSC values. CSC values for Ni939 and Ni939+1.5Si samples are similar; however, Ni939+1.5Si sample shows shorter cracks and lower crack density [Fig. 2(b), (c)]. This observation indicates the discrepancy between experimental results and CSC prediction for Ni939 and Ni939+1.5Si samples, which needs another explanation.

Solidification processes describing temperature (T) vs. f_s for the four samples were simulated with Scheil Solidification Simulation Model [Fig. 3(b)]. The relaxed range (liquid phase from 60 to 10%) and vulnerable-to-cracking range (liquid phase between 10 and 1%) are marked. Clearly, solidification temperature of Ni939+7.4Si is distinctively sensitive to f_s (significantly higher steepness) in the vulnerable-to-cracking period. Kou^[30] proposed a cracking criterion based on strain rate, which was focused on the sensitivity of last fraction of liquid to solidify before reaching solidus temperature. This prediction of cracking is based on the maximum steepness of the $f_s^{1/2}$ vs. T curves, described by $|dT/df_s^{1/2}|$. The larger the $|dT/df_s^{1/2}|$ value, the higher tendency the material cracks. With this criterion, the maximum steepness of the curves with the corresponding f_s where the data were calculated are listed in Table I, which is in good agreement with

the crack densities observed for the Ni939, Ni939+1.5Si, and Ni939+7.4 samples (Fig. 2(b), (c), (e)). However, no significant difference of $\left|dT/df_s^{1/2}\right|$ between Ni939+2.8Si and Ni939 or Ni939+1.5Si sample is observed, not accurately reflecting the remarkable cracking resistance improvement for the Ni939+2.8Si sample. Therefore, a combination of CSC prediction and $\left|dT/df_s^{1/2}\right|$ value can be a better indicator for cracking resistance of Inconel 939 alloy with Si additions. And the reason for the significantly higher cracking tendency for the Ni939+7.4Si sample is the relatively long time the material remains over the vulnerable-to-cracking stage with significantly high strain rate. Similarly, the remarkably improved cracking resistance of Ni939+2.8Si is attributed to the clearly reduced time under the vulnerable-to-cracking stage.

Conclusions

In this study, Si was added into Inconel 939 alloy aiming to improve the cracking resistance under laser additive manufacturing conditions. Thermo-Calc software was utilized to guide composition selection, and experimental studies were performed to verify the simulation results. The following two conclusions are reached.

- (1) The amounts of boundary strengthening elements, namely C, B and Zr, in liquid phase of Inconel 939 alloy decrease with the increase of Si addition during solidification. However, the contents of elements C, B and Zr alone is not adequate to determine cracking tendency. In comparison, cracking susceptibility coefficient prediction together with $\left|dT/df_s^{1/2}\right|$ calculation by Thermo-Calc is a better cracking resistance indicator for Inconel 939 alloy with Si additions.
- (2) With a Si addition of around 2.8 wt%, solidification cracking resistance of Inconel 939 alloy is significantly improved and no visible cracks are observed on the laser processed surface.

The success of making crack-free Inconel 939 alloy suitable for laser AM process with Si addition is inspiring. The computational thermodynamics method approach shown in this study can be applied to guide the composition modifications for other non-weldable alloys, to make them suitable for laser AM process if the cracking mechanism is dominated by solidification cracking.

Acknowledgments

This work is supported by the US National Science Foundation under Grant OIA-1946231 and the Louisiana Board of Regents for the Louisiana Materials Design Alliance (LAMDA). CZ and

SG are also partially supported by U.S. Department of Energy under Award Number DE-SC0019378.

Data availability

The datasets generated during and/or analyzed during the current study are available from the corresponding author on reasonable request.

Declarations

Conflict of interest

The authors declare that they have no known competing financial interests or personal relationships that could have appeared to influence the work reported in this paper.

Open Access

This article is licensed under a Creative Commons Attribution 4.0 International License, which permits use, sharing, adaptation, distribution and reproduction in any medium or format, as long as you give appropriate credit to the original author(s) and the source, provide a link to the Creative Commons licence, and indicate if changes were made. The images or other third party material in this article are included in the article's Creative Commons licence, unless indicated otherwise in a credit line to the material. If material is not included in the article's Creative Commons licence and your intended use is not permitted by statutory regulation or exceeds the permitted use, you will need to obtain permission directly from the copyright holder. To view a copy of this licence, visit <http://creativecommons.org/licenses/by/4.0>.

References

1. R. Singh, A. Gupta, O. Tripathi, S. Srivastava, B. Singh, A. Awasthi, S. Rajput, P. Sonia, P. Singhal, K.K. Saxena, Powder bed fusion process in additive manufacturing: an overview. *Mater. Today: Proc.* **26**, 3058–3070 (2020)
2. M. Delic, D.R. Eyers, The effect of additive manufacturing adoption on supply chain flexibility and performance: an empirical analysis from the automotive industry. *Int. J. Product. Econ.* **228**, 107689 (2020)
3. M. Revilla-León, M. Sadeghpour, M. Özcan, A review of the applications of additive manufacturing technologies used to fabricate metals in implant dentistry. *J. Prosthodontics* **29**(7), 579–593 (2020)
4. A. Hemmasian Etefagh, C. Zeng, S. Guo, J. Raush, Corrosion behavior of additively manufactured Ti-6Al-4V parts and the effect of post annealing. *Addit. Manuf.* **28**, 252–258 (2019)
5. O. Gokcekaya, T. Ishimoto, S. Hibino, J. Yasutomi, T. Narushima, T. Nakano, Unique crystallographic texture formation in Inconel 718 by laser powder bed fusion and its effect on mechanical anisotropy. *Acta Mater.* **212**, 116876 (2021)
6. G. Marchese, S. Parizia, M. Rashidi, A. Saboori, D. Manfredi, D. Ugues, M. Lombardi, E. Hryha, S. Biamino, The role of texturing and microstructure evolution on the tensile behavior of heat-treated Inconel 625 produced via laser powder bed fusion. *Mater. Sci. Eng. A* **769**, 138500 (2020)
7. A.E. Wilson-Heid, S. Qin, A.M. Beese, Multiaxial plasticity and fracture behavior of stainless steel 316L by laser powder bed fusion: experiments and computational modeling. *Acta Mater.* **199**, 578–592 (2020)
8. P. Lassègue, C. Salvan, E. De Vito, R. Soulas, M. Herbin, A. Hemberg, T. Godfroid, T. Baffie, G. Roux, Laser powder bed fusion (L-PBF) of Cu and

- CuCrZr parts: Influence of an absorptive physical vapor deposition (PVD) coating on the printing process. *Addit. Manuf.* **39**, 101888 (2021)
9. A.S. Shaikh, Development of a γ' Precipitation Hardening Ni-Base Superalloy for Additive Manufacturing, 2018.
 10. M.G. Albarrán, D. Martínez, E. Díaz, J. Díaz, I. Guzman, E. Saucedo, A.M. Guzman, Effect of preweld heat treatment on the microstructure of heat-affected zone (HAZ) and weldability of Inconel 939 superalloy. *J. Mater. Eng. Perform.* **23**(4), 1125–1130 (2014)
 11. S. Shaw, Response of IN-939 to process variations. *Superalloys* **1980**, 275–284 (1980)
 12. J. Zhu, A. Wise, T. Nuhfer, G.R. Holcomb, P.D. Jablonski, S. Sridhar, D.E. Laughlin, High-temperature-oxidation-induced ordered structure in Inconel 939 superalloy exposed to oxy-combustion environments. *Mater. Sci. Eng. A* **566**, 134–142 (2013)
 13. B. Dovggy, M. Simonelli, M.-S. Pham, Alloy design against the solidification cracking in fusion additive manufacturing: an application to a FeCrAl alloy. *Mater. Res. Lett.* **9**(8), 350–357 (2021)
 14. J.C. Lippold, *Welding Metallurgy and Weldability* (Wiley, New York, 2014)
 15. K. Saida, H. Matsushita, K. Nishimoto, K. Kiuchi, J. Nakayama, Quantitative influence of minor and impurity elements on hot cracking susceptibility of extra high-purity type 310 stainless steel. *Yosetsu Gakkai Ronbunshu* **31** (2013).
 16. G. Agarwal, A. Kumar, H. Gao, M. Amirthalingam, S.C. Moon, R.J. Dippenaar, I. Richardson, M. Hermans, Study of solidification cracking in a transformation-induced plasticity-aided steel. *Metall. Mater. Trans. A* **49**(4), 1015–1020 (2018)
 17. J. Zhang, B. Song, Q. Wei, D. Bourell, Y. Shi, A review of selective laser melting of aluminum alloys: processing, microstructure, property and developing trends. *J. Mater. Sci. Technol.* **35**(2), 270–284 (2019)
 18. P. KondaGokuldoss, Work hardening in selective laser melted Al-12Si alloy. *Mater. Des. Process. Commun.* **1**(2), e46 (2019)
 19. N. Takata, M. Liu, H. Kodaira, A. Suzuki, M. Kobashi, Anomalous strengthening by supersaturated solid solutions of selectively laser melted Al-Si-based alloys. *Addit. Manuf.* **33**, 101152 (2020)
 20. M.L. Montero-Sistiaga, R. Mertens, B. Vrancken, X. Wang, B. Van Hooreweder, J.-P. Kruth, J. Van Humbeeck, Changing the alloy composition of Al7075 for better processability by selective laser melting. *J. Mater. Process. Technol.* **238**, 437–445 (2016)
 21. J.C. Lippold, S.D. Kiser, J.N. DuPont, *Welding Metallurgy and Weldability of Nickel-Base Alloys* (Wiley, New York, 2011)
 22. H. Hyer, L. Zhou, A. Mehta, S. Park, T. Huynh, S. Song, Y. Bai, K. Cho, B. McWilliams, Y. Sohn, Composition-dependent solidification cracking of aluminum-silicon alloys during laser powder bed fusion. *Acta Mater.* **208**, 116698 (2021)
 23. X. Yu, X. Lin, F. Liu, L. Wang, Y. Tang, J. Li, S. Zhang, W. Huang, Influence of post-heat-treatment on the microstructure and fracture toughness properties of Inconel 718 fabricated with laser directed energy deposition additive manufacturing. *Mater. Sci. Eng. A* **798**, 140092 (2020)
 24. H. Wen, C. Zeng, A. Hemmasian Etefagh, J. Gao, S. Guo, Laser surface treatment of Ti-10Mo alloy under Ar and N₂ environment for biomedical application. *J. Laser Appl.* **31**(2), 022012 (2019)
 25. A.K. Syed, B. Ahmad, H. Guo, T. Machry, D. Eatock, J. Meyer, M.E. Fitzpatrick, X. Zhang, An experimental study of residual stress and direction-dependence of fatigue crack growth behaviour in as-built and stress-relieved selective-laser-melted Ti6Al4V. *Mater. Sci. Eng. A* **755**, 246–257 (2019)
 26. Z.-C. Fang, Z.-L. Wu, C.-G. Huang, C.-W. Wu, Review on residual stress in selective laser melting additive manufacturing of alloy parts. *Opt. Laser Technol.* **129**, 106283 (2020)
 27. T. Clyne, C. TW, The influence of composition on solidification cracking susceptibility in binary alloy systems (1981)
 28. F. Yan, J. Yan, D. Linder, Understanding hot cracking of steels during rapid solidification: an ICME approach. *Mater. Proc.* **3**, 30 (2021)
 29. X. Yan, J.C. Lin, Prediction of hot tearing tendency for multicomponent aluminum alloys. *Metall. Mater. Trans. B* **37**(6), 913–918 (2006)
 30. S. Kou, A criterion for cracking during solidification. *Acta Mater.* **88**, 366–374 (2015)